ELECTRONIC SUPPLEMENTARY INFORMATION

Finally, inkjet-printed metal halide perovskite LEDs – utilizing seed crystal templating of salty PEDOT:PSS

Felix Hermerschmidt,[†a] Florian Mathies,[†b] Vincent R. F. Schröder,[a] Carolin Rehermann,[b] Nicolas Zorn Morales,[a] Eva L. Unger [b,c] and Emil J. W. List-Kratochvil *[a,d]

[a.] Humboldt-Universität zu Berlin, Institut für Physik, Institut für Chemie, IRIS Adlershof, Brook-Taylor-Straße 6, 12489 Berlin, Germany. Email: emil.list-kratochvil@hu-berlin.de

[b.] Young Investigator Group Hybrid Materials Formation and Scaling, Helmholtz-Zentrum Berlin für Materialen und Energie GmbH, Kekuléstraße 5, 12489 Berlin, Germany.

[c.] Chemical Physics and NanoLund, Lund University, PO Box 124, 22100 Lund, Sweden.

[d.] Helmholtz-Zentrum, Berlin für Materialien und Energie GmbH, Brook-Taylor-Straße 6, 12489 Berlin, Germany.

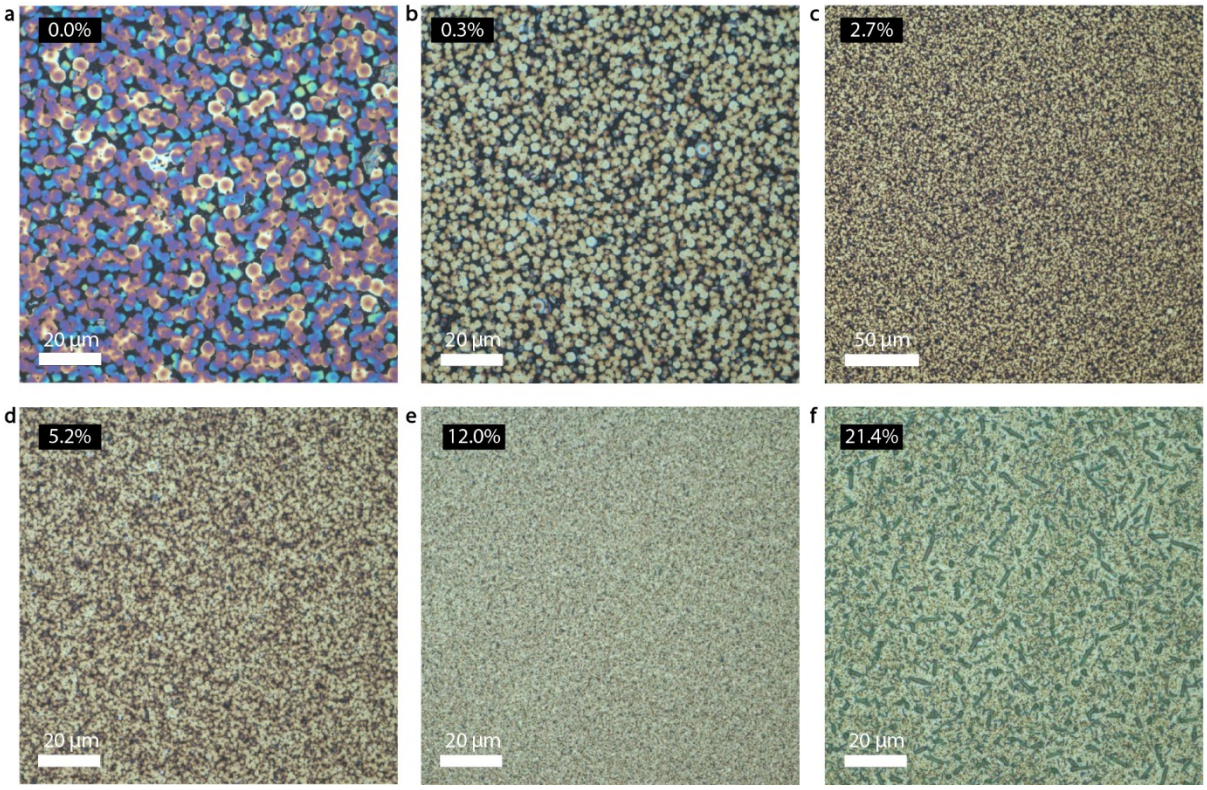

Figure S1: The optical microscopy images of $MAPbBr_3$:PEG composite blended with **a** 0.0%, **b** 0.3%, **c** 2.7%, **d** 5.2%, **e** 12.0% and **f** 21.4% PEG show optimum homogeneous morphology at 12.0% PEG addition.

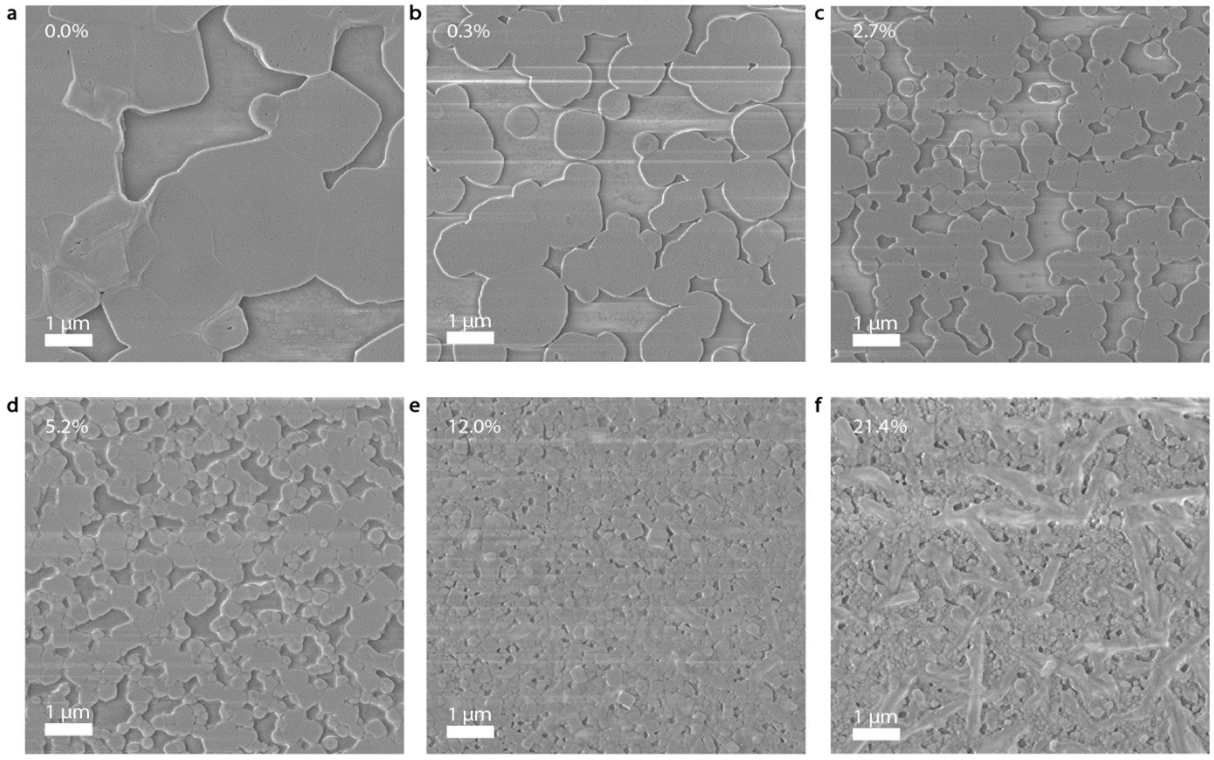

Figure S2: The scanning electron microscopy images of $MAPbBr_3$:PEG composite blended with **a** 0.0%, **b** 0.3%, **c** 2.7%, **d** 5.2%, **e** 12.0% and **f** 21.4% PEG confirm the optimum morphology for 12.0% PEG.

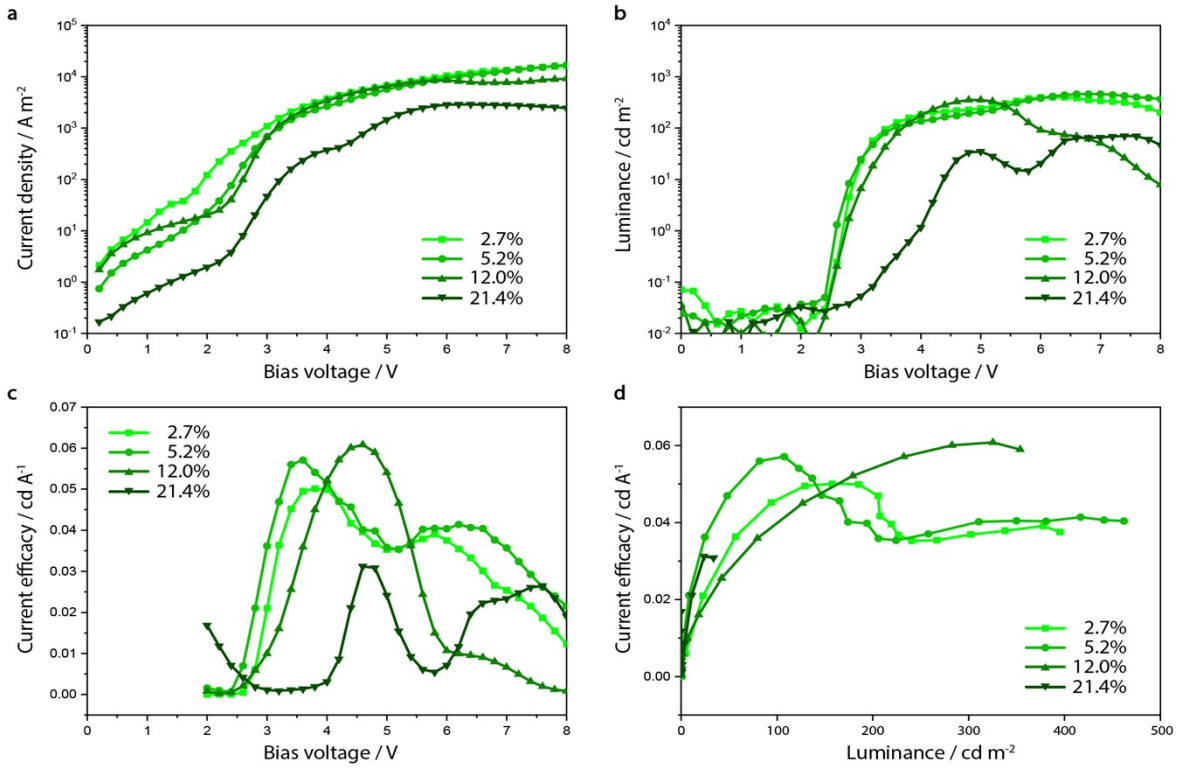

Figure S3: Also the device performance parameters for PeLEDs incorporating $MAPbBr_3$ perovskite active layer blended with 2.7%, 5.2%, 12.0% and 21.4% PEG, respectively, show optimum performance with 12% PEG content.

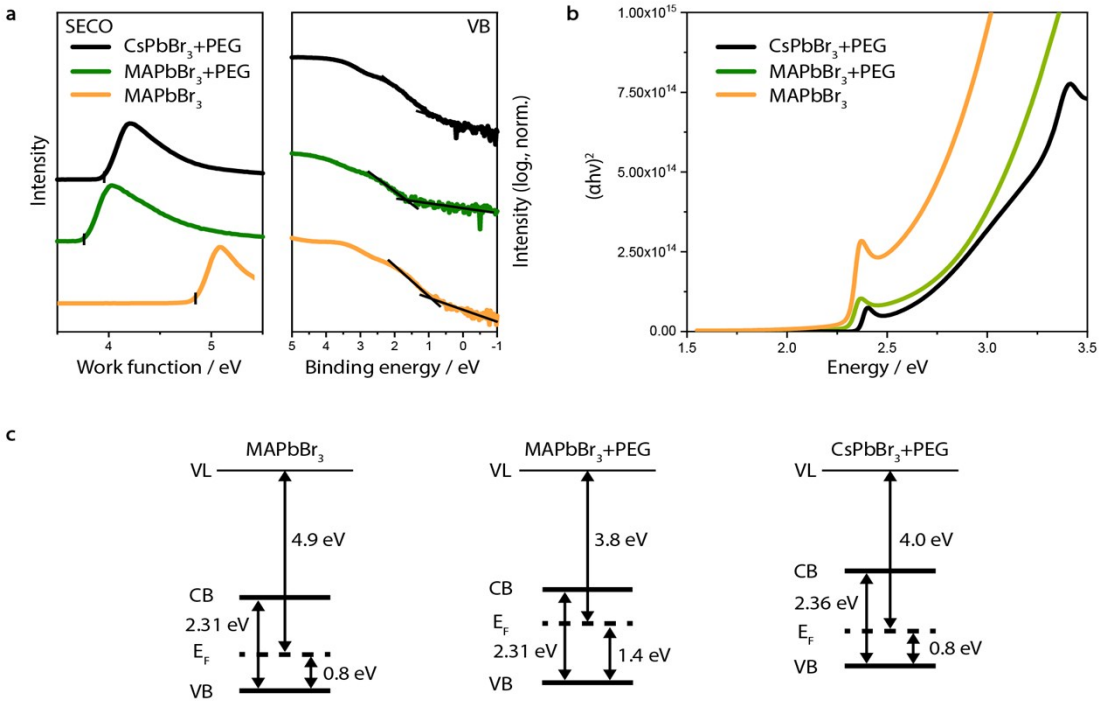

Figure S4: **a** The secondary electron cut-off and valence band on-set, **b** Tauc plots based on UV-vis absorption spectroscopy and **c** schematic of energy levels for $MAPbBr_3$, $MAPbBr_3$:PEG and $CsPbBr_3$:PEG resulting from the experimental data.

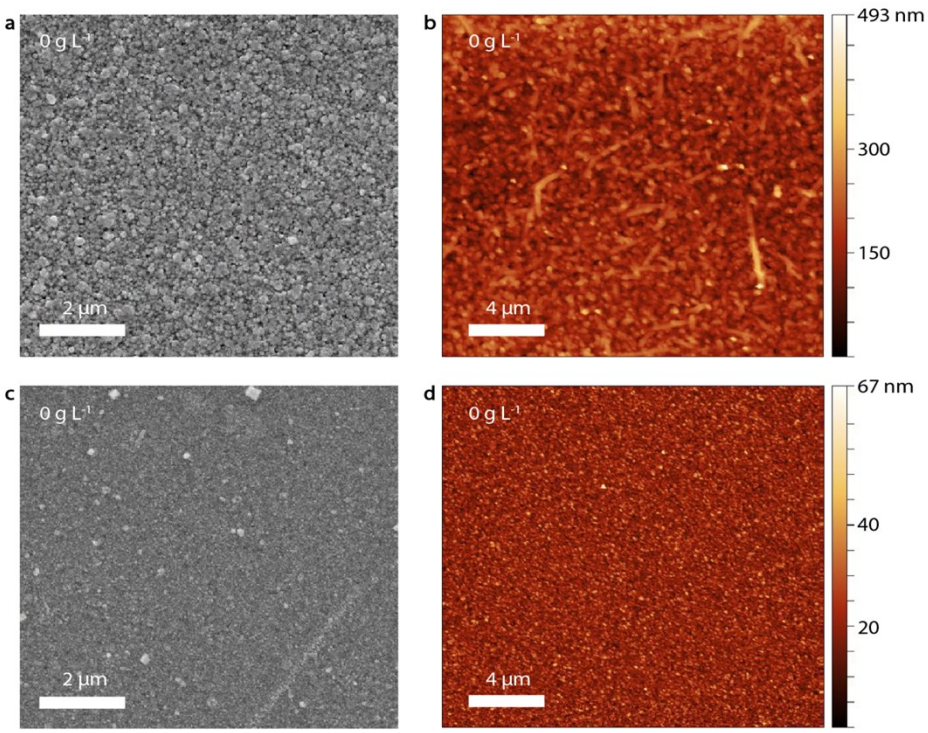

Figure S5: The SEM and SFM images of spin-coated (**a**, **b**) and inkjet-printed (**c**, **d**) $MAPbBr_3$:PEG composite films on pristine PEDOT:PSS (without KCl) confirm the pinhole-free active layer morphology achievable from the two processing methods.

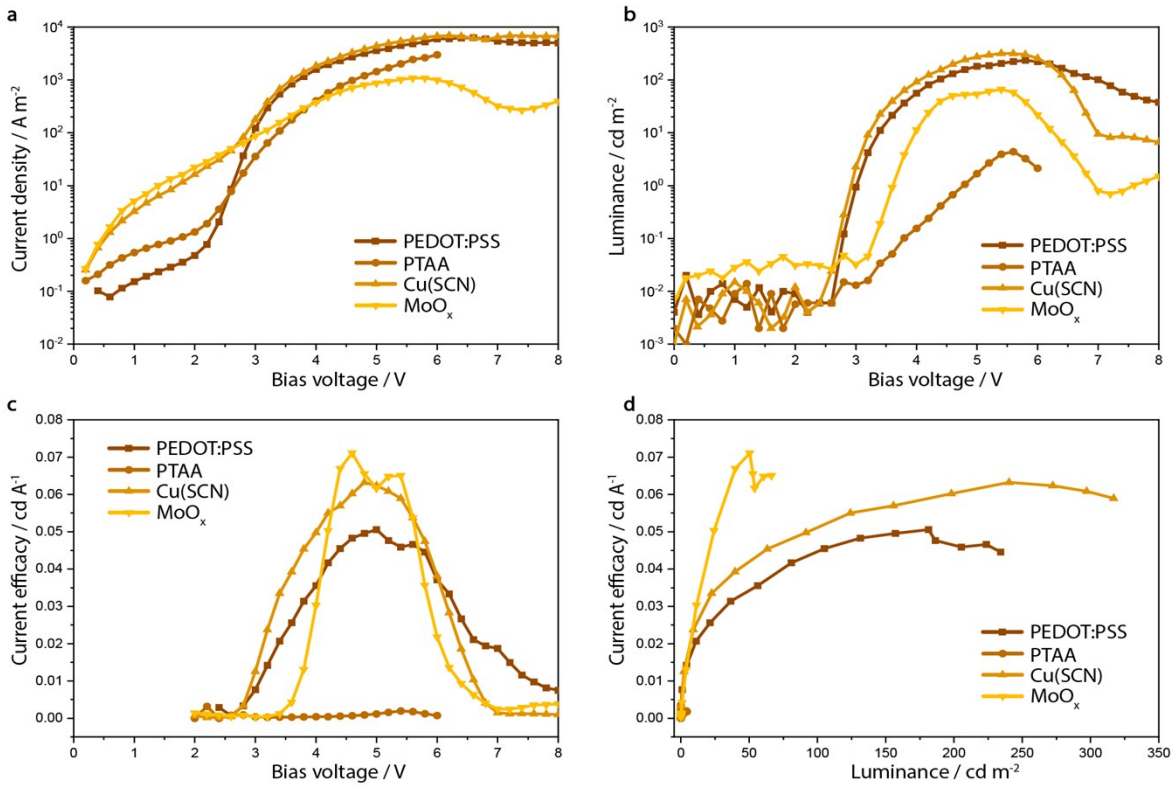

Figure S6: $MAPbBr_3$:PEG-based devices were produced on pristine PEDOT:PSS or molybdenum oxide (**MoO_x**) as HIL as well as PEDOT:PSS plus either poly[bis(4-phenyl)(2,4,6-trimethylphenyl)amine] (**PTAA**) and cuprous thiocyanate (**CuSCN**). Stark contrasts are seen, with only the processing on pristine PEDOT:PSS yielding devices that show the best combination of low leakage current and reasonable device luminance. Devices with $MAPbBr_3$:PEG active layer processed on pristine PTAA and Cu(SCN) failed to function due to low wetting on PTAA and washing away of CuSCN during processing. PeLEDs including MoOx layer showed degradation during operation due to interactions between MoOx and the $MAPbBr_3$:PEG composite layer.

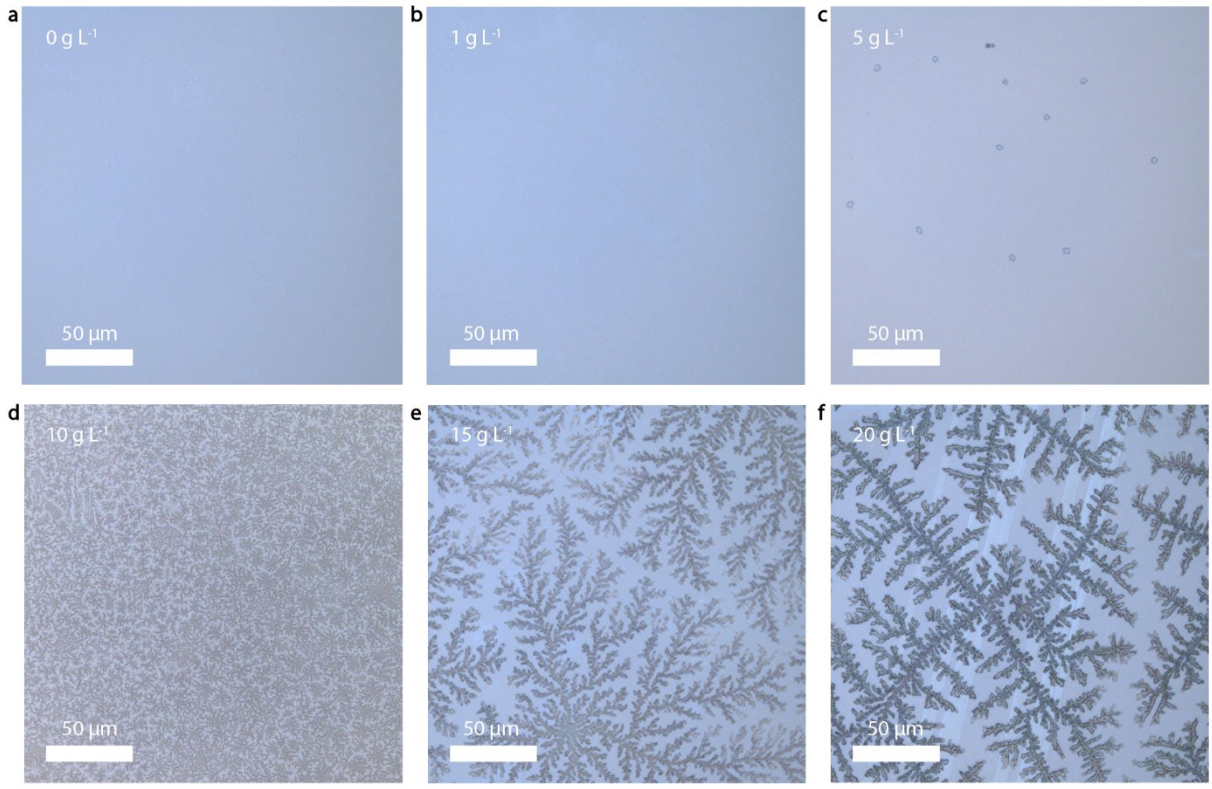

Figure S7: The series of optical microscope images of the PEDOT:PSS layer with increasing amounts of KCl shows the increasingly large dendritic structures of the KCl.

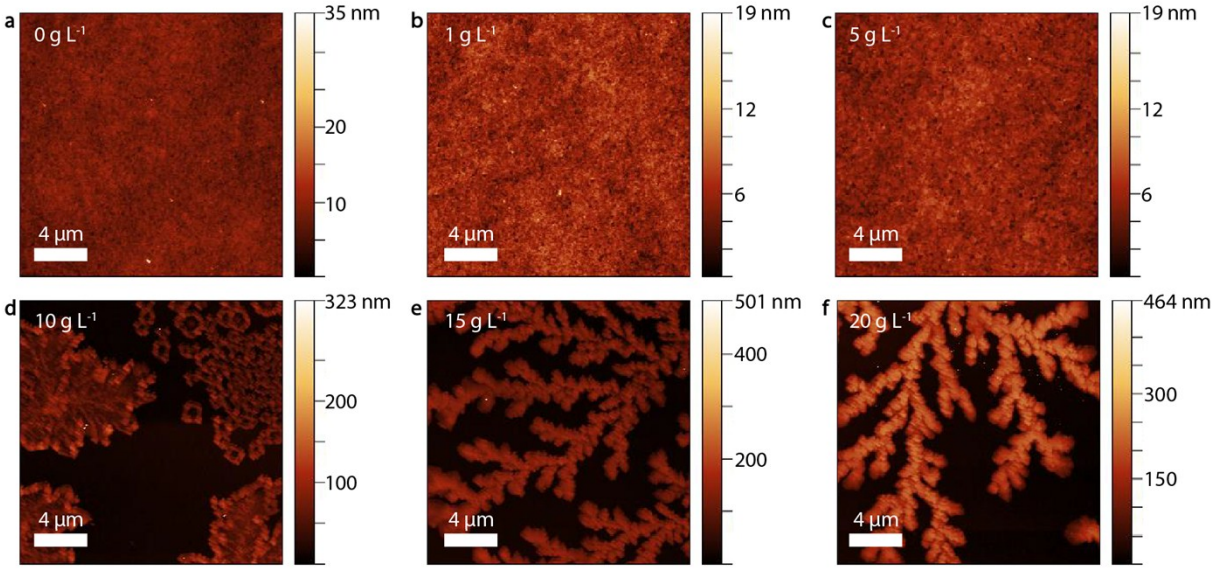

Figure S8: The dendritic structures are confirmed in SFM images of PEDOT:PSS incorporating increasing amounts of KCl.

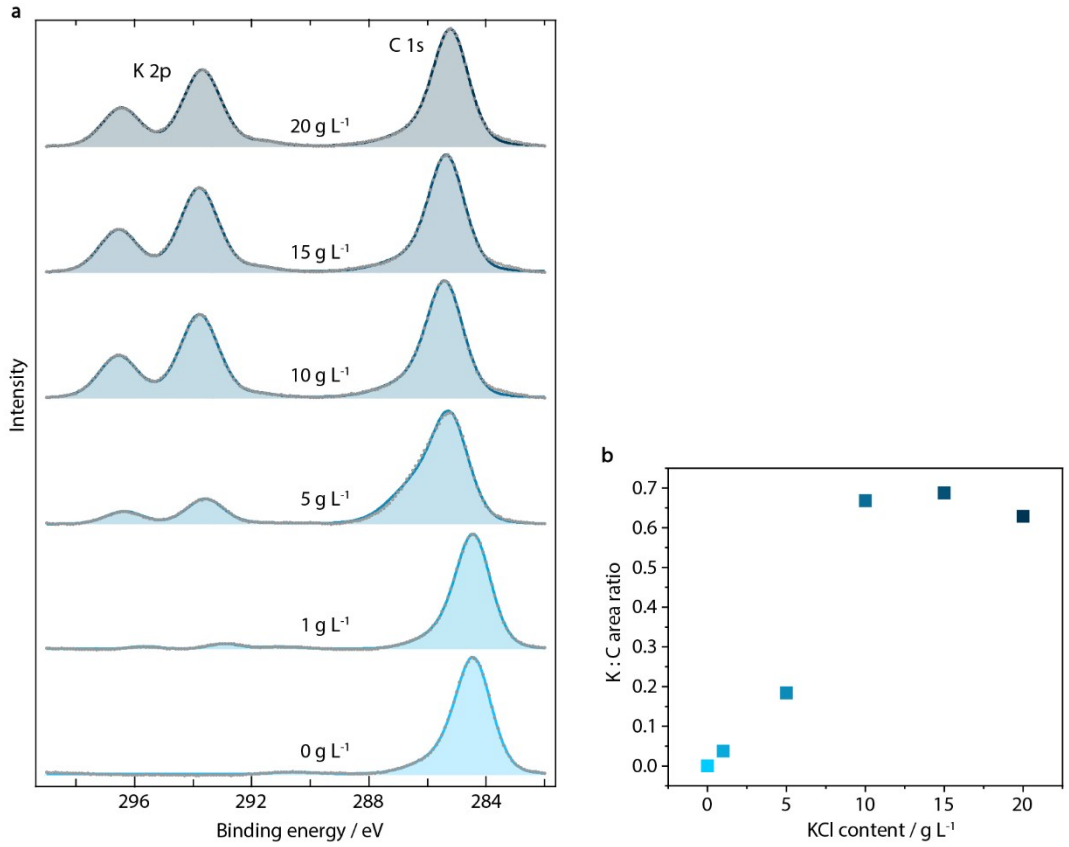

Figure S9: **a** XPS spectra show the increasing K 2p peak (doublet at 295 eV, corresponding to the added KCl) and the C 1s peak (285 eV, corresponding to the PEDOT:PSS surface), **b** the K:C area ratios show the saturation at high KCl content.

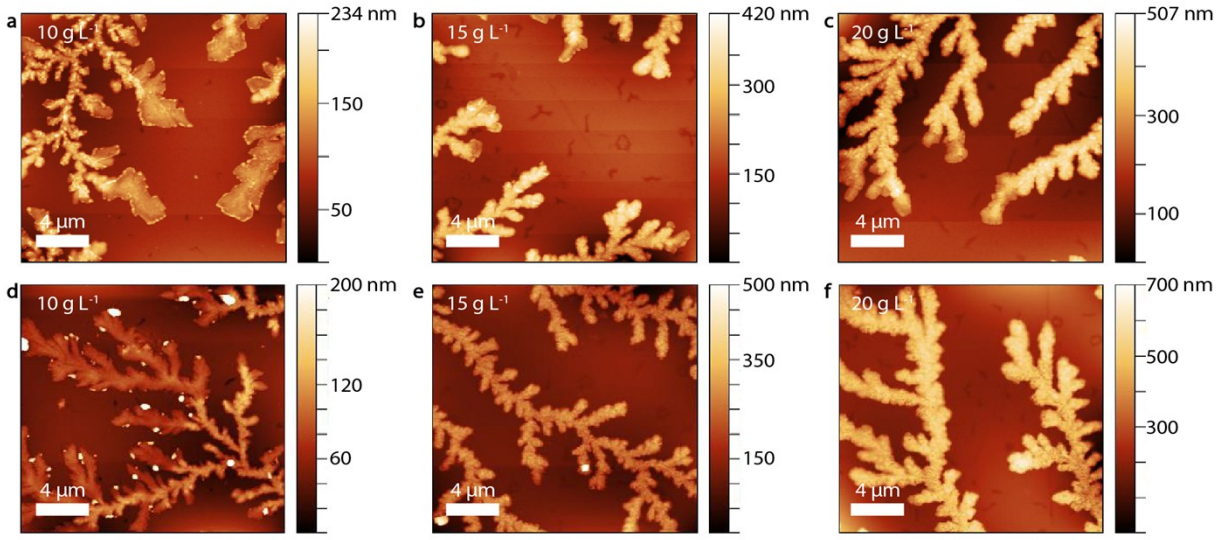

Figure S10: The SFM images of PEDOT:PSS layers containing KCl before and after washing with the solvent used for perovskite deposition show no noticeable change in the dendritic structures visible.

Table S1: This is confirmed in the feature heights measured before and after washing.

	0 g L^{-1}	1 g L^{-1}	5 g L^{-1}	10 g L^{-1}	15 g L^{-1}	20 g L^{-1}
pre washing	-	-	-	~100 nm	~250 nm	~330 nm
post washing	-	-	-	~50 nm	~210 nm	~300 nm

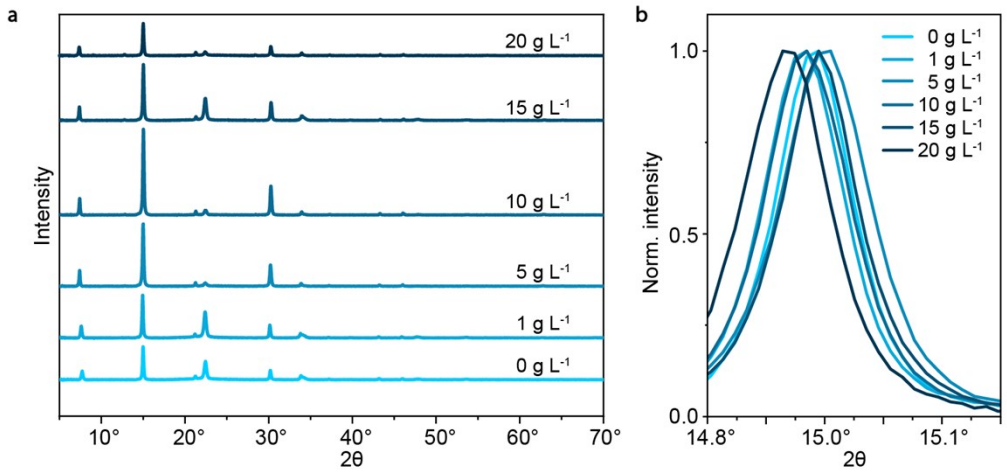

Figure S11: **a** XRD diffraction patterns of the full series of $MAPbBr_3$:PEG-composite spin-coated on PEDOT:PSS/KCl with increasing KCl concentration indicate no apparent shift in the diffraction peaks. The diffraction peaks at 7.5° and 22.5° most likely result from the PEG. **b** No trend in shift of the magnified predominant [100] $MAPbBr_3$ diffraction peak is visible as a function of KCl content.

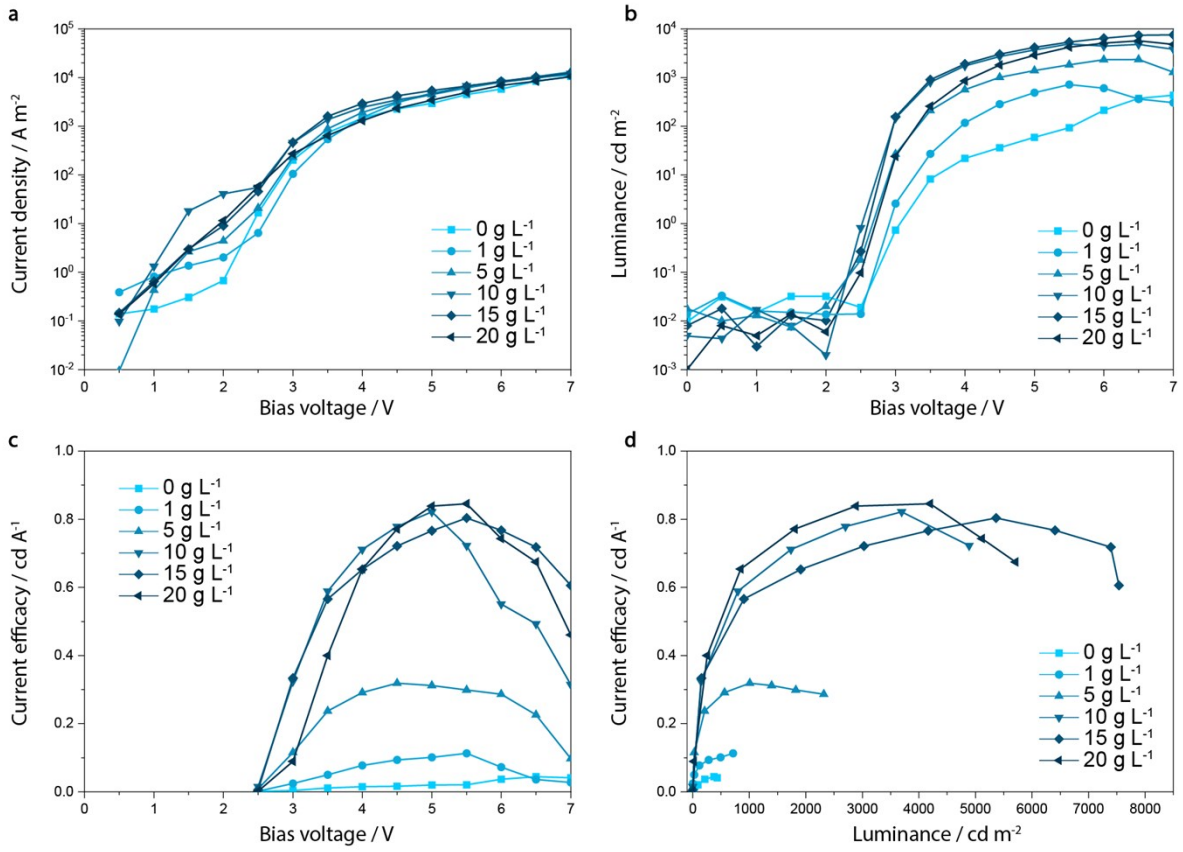

Figure S12: The current density / voltage / luminance curves of spin coated devices incorporating varying amounts of KCl within the PEDOT:PSS HIL show the rising luminance and current efficacy (cd A^{-1}) as a function of incorporated KCl. While the absolute maximum efficacy is achieved by devices incorporating 20 g L^{-1} KCl, this maximum is only marginally greater than that obtained from devices incorporating 15 g L^{-1} KCl, but at the expense of a much lower luminance.

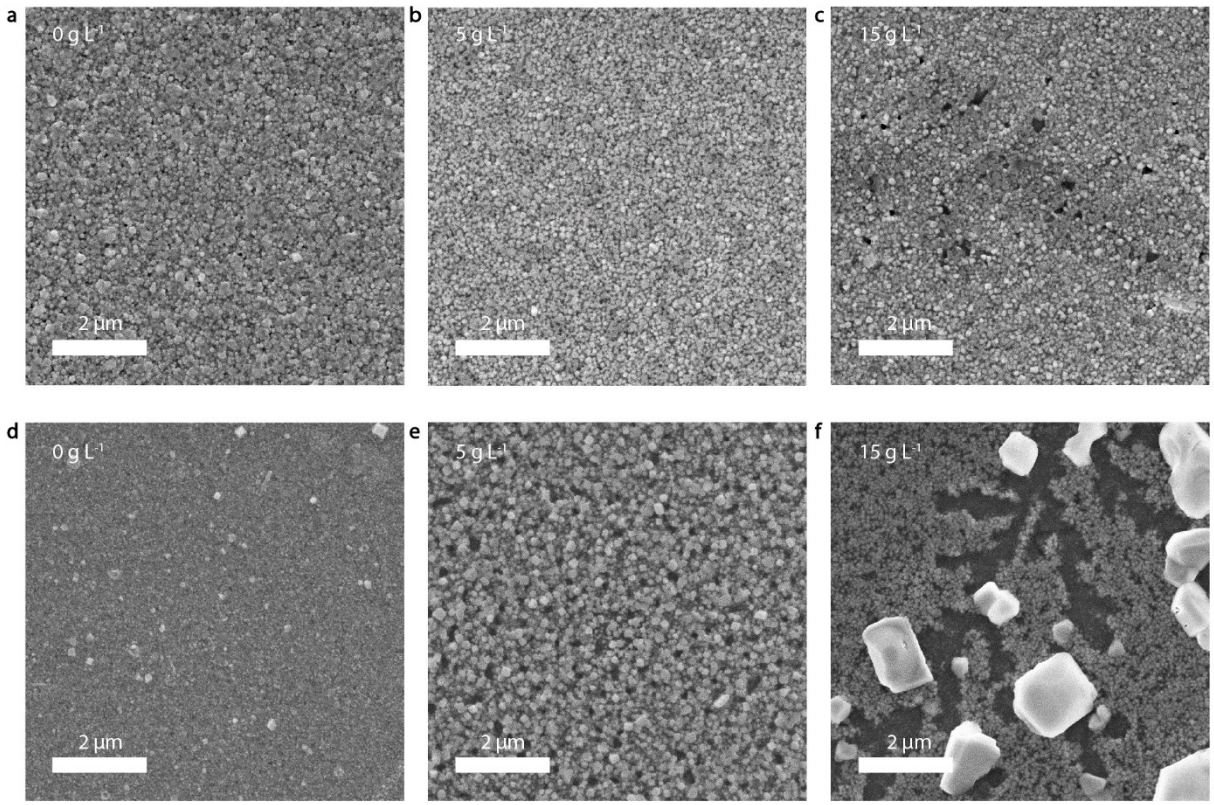

Figure S13: The SEM images of $MAPbBr_3$:PEG-composite spin-coated (top row **a**-**c**) and inkjet-printed (bottom row **d**-**f**) on PEDOT:PSS/KCl show different effects when increasing KCl concentration from 0 g L^{-1} to 5 g L^{-1} to 15 g L^{-1}. While similar morphology is seen for spin-coated and inkjet-printed layers at KCl concentrations of 15 g L^{-1} (**c**) and 5 g L^{-1} (**e**), respectively, a substantial difference in morphology is observed for layers inkjet-printed on PEDOT:PSS containing 15 g L^{-1}. This leads to the two different optimums achieved in PeLED device performance described in the main text.

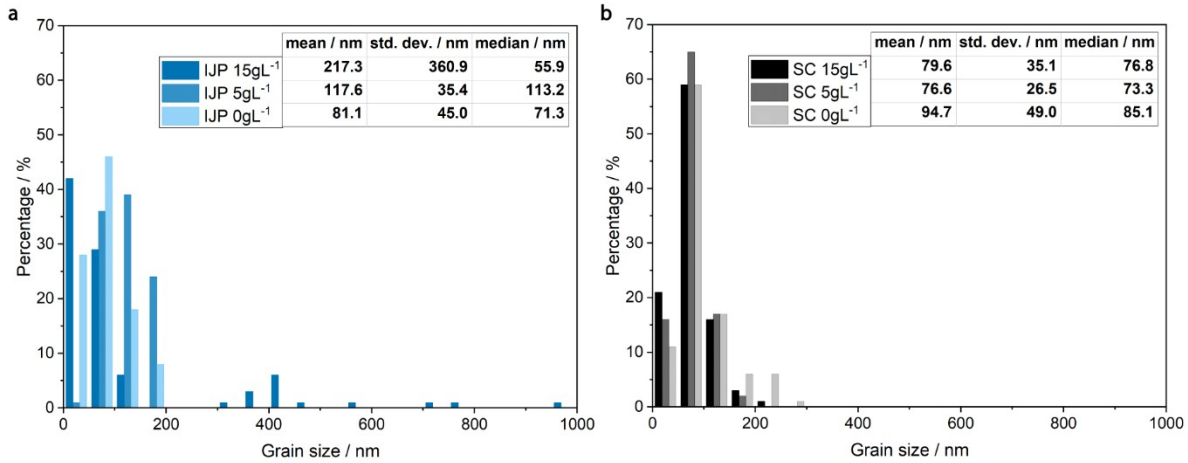

Figure S14: Upon increasing the KCl content, smaller average grains are seen for spin-coated devices. Additionally, the standard deviation decreases, signifying a more homogeneous film. For inkjet-printed films, the mean grain size increases with increasing KCl content. But while at 5 g L^{-1} the standard deviation is also lower, indicating a more homogenous film, for the high KCl content of 15 g L^{-1} these values have to be taken with care, as some micrometer large grains distort the calculations.